Journal of Materials Chemistry A

COMMUNICATION

View Article Online
View Journal | View Issue

Cite this: J. Mater. Chem. A, 2017, 5, 1930

Received 14th November 2015
Accepted 15th December 2015

DOI: 10.1039/c5ta09232a

www.rsc.org/MaterialsA

Nanocarbon-intercalated and Fe–N-codoped graphene as a highly active noble-metal-free bifunctional electrocatalyst for oxygen reduction and evolution†

Daping He,[abc] Yuli Xiong,[c] Jinlong Yang,[a] Xu Chen,[a] Zhaoxiang Deng,*[b] Mu Pan,[a] Yadong Li[bd] and Shichun Mu*[a]

We report a rationally designed electrocatalyst with high activity for both the oxygen reduction reaction (ORR) and oxygen evolution reaction (OER) based on a nanocarbon-intercalated graphene (CIG) material doped with nitrogen (N) and iron (Fe) (Fe–N-CIG). This easily made novel 3D Fe–N-CIG catalyst exhibits a surprisingly high ORR and OER activity and stability, making it a new noble-metal-free bifunctional catalyst for future applications in regenerative energy conversion systems.

Energy crisis has aroused tremendous and continuous research interest in finding sustainable energy conversion systems with high efficiency and low cost.[1–3] Catalysts towards electrochemical oxygen reduction and evolution reactions play a central role in renewable energy related technologies.[4,5] Usually, the oxygen reduction reaction (ORR) with a reasonably low overpotential on the cathode side is a vital issue for fuel cells.[6,7] On the other hand, the oxygen evolution reaction (OER) on an anode lies at the heart of electrochemical water splitting and metal–air batteries.[8–10] Currently, Pt and its alloys are the most active catalysts for the ORR,[11–14] while ruthenium and iridium oxides are the best OER catalysts.[15,16] However, a widespread use of these catalysts will accelerate the consumption of the rarest elements on earth, and thus hinder their industrialization. As a result, intensive research has been focused on reducing the use of noble metals in ORR and OER catalysts but still maintaining similar or even higher activities. Some other efforts intend to improve catalyst stability and increase catalyst utilization. Among these pursuits, one important trend is to develop noble-metal-free materials for ORR and OER applications, including earth abundant metal-based or metal-free catalysts.[9,10,17–20] However, finding a noble-metal-free electrocatalyst possessing high activities for both the ORR and OER is very challenging, which has been rarely reported.[4,21,22] Such a dual-function catalyst is of great significance for rechargeable metal–air batteries or unitized regenerative fuel cells (URFCs) capable of working as a fuel cell to form water and in reverse as a water electrolyzer producing H_2 and O_2 to refeed the fuel cell.[4,20]

In response to the urgent demand for reduced use of noble metals in both ORR and OER catalysts, nitrogen-doped carbon materials have shown great promise due to their high catalytic activity, zero consumption of noble metals, and environmental friendliness.[17–20] In particular, N-doped graphene (N-G) has drawn special attention recently, largely due to its high surface area, excellent thermal and electrical conductivities, and superior mechanical and chemical stabilities,[21–24] which make N-G attractive as a high performance ORR or OER catalyst.[10,25–28] However, the existence of strong π–π stacking interactions between graphene nanosheets (GNSs) often results in irreversible agglomerates of graphene layers,[23,29] causing a loss of their unique 2D structure. This effect significantly reduces the surface area and limits the permeation of the electrolyte between graphene layers. As a result, catalytically active sites generated upon N-doping would be largely compromised, forming a serious barrier for graphene-based materials as active electrocatalysts.

In the present work, we report on a conductive nanocarbon-intercalated nitrogen-doped graphene material containing trace amounts of iron (Fe–N-CIG) as a high performance ORR and OER dual-functional catalyst (Fig. 1). The existence of interplanar carbon nanospheres (CNSs) in the graphene-based structures provides abundant electrolyte channels which are expected to facilitate the diffusion of reactive species to catalytically active sites. In addition, the carbon nanospheres can serve as "shortcuts" for interplanar electron transport, and thus guarantee a good conductivity of the materials. The resulting

[a]State Key Laboratory of Advanced Technology for Materials Synthesis and Processing, Wuhan University of Technology, Wuhan 430070, China. E-mail: msc@whut.edu.cn
[b]Center of Advanced Nanocatalysis (CAN-USTC), University of Science and Technology of China, Hefei 230002, China. E-mail: zhxdeng@ustc.edu.cn
[c]Department of Chemistry, University of Bath, Bath, Somerset BA2 7AY, UK
[d]Department of Chemistry, Tsinghua University, Beijing 100084, China

† Electronic supplementary information (ESI) available: Details of catalyst synthesis, electrochemical measurements, and extra supporting data. See DOI: 10.1039/c5ta09232a

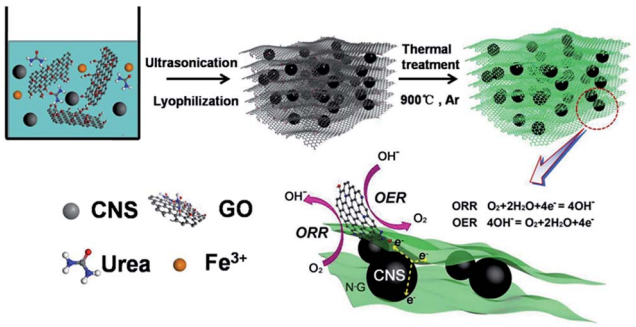

Fig. 1 Schematic illustration of a synthetic process for Fe–N-CIG which shows enhanced catalytic activities for both the ORR and OER.

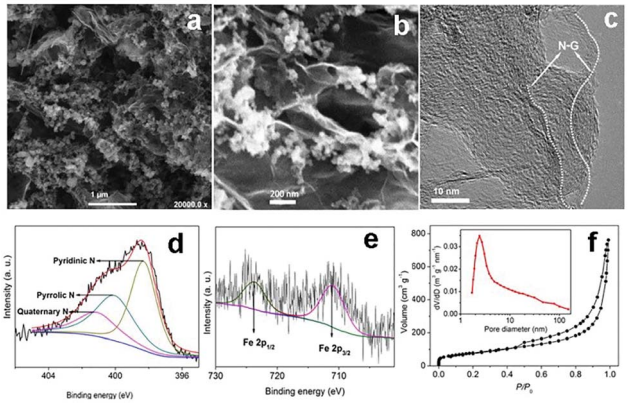

Fig. 2 Characterization of Fe–N-CIG hybrid materials. (a and b) SEM images under different magnifications of the Fe–N-CIG hybrid drop-coated on a silicon substrate from its aqueous suspension. (c) High magnification TEM image of the Fe–N-CIG hybrid. Dotted lines indicate the edges of two N-doped graphene (N-G) layers. (d and e) High-resolution XPS N 1s (d) and Fe 2p (e) spectra of Fe–N-CIG. (f) The nitrogen adsorption/desorption isotherm along with a pore size distribution (inset) of the Fe–N-CIG catalyst.

Fe–N-CIG catalyst exhibits higher ORR activity and enhanced stability in an alkaline medium, in comparison with a commercial Pt/C catalyst (Johnson Matthey Corp., 20 wt% Pt on Vulcan XC-72). In the meantime, the Fe–N-CIG shows an excellent OER activity with an onset potential of at least 100 mV lower than that of iridium oxide (IrO_2), a well-known precious metal-based catalyst for electrochemical water oxidation.

As shown in Fig. 1, the Fe–N-CIG catalyst was synthesized by a simple two-step process. In the first step, urea, ferric ammonium sulfate, and CNS (Vulcan XC-72, Cabot Co., washed with 1 M H_2SO_4 before use) were added to an aqueous solution of graphene oxide (GO). The mixture was thoroughly dispersed with the assistance of ultrasonication, and then dried by rotary evaporation and subsequent lyophilization. In the second step, the lyophilized solid was subjected to a thermal treatment at 900 °C in an argon flow. This resulted in an N and Fe co-doped and thermally reduced GO material with a nanocarbon-intercalated three dimensional (3D) structure (Fe–N-CIG) (see ESI† for details).

The special architecture of the nanosphere/nanosheet composite was confirmed by scanning electron microscopy (SEM) (Fig. 2a and b) and transmission electron microscopy (TEM) (Fig. 2c). The SEM and TEM data showed that the Vulcan XC-72 carbon nanospheres formed a good nano-composite with the N-doped graphene nanosheets (GNSs). In contrast, the N-doped graphene material containing trace amounts of iron in the absence of CNS (Fe–N-G, a control sample) showed a closely restacked multilayer GNS structure with crumpled morphologies (Fig. S1†). X-ray photoelectron spectroscopy (XPS) revealed an existence of 7.39 at% nitrogen in the Fe–N-CIG, which was greater than that in the Fe–N-G sample (3.21 at%, Fig. S2 and S3†). This probably meant that the intercalated Fe–N-CIG structure could facilitate N doping reactions. The high resolution XPS N 1s spectrum could be deconvoluted into three sub-peaks which disclosed the presence of pyridinic (398.6 eV), pyrrolic (400.2 eV), and quaternary nitrogen (401.3 eV) species in the Fe–N-CIG structure (Fig. 2d).[30] The Fe–N-CIG showed a higher ratio of pyridinic N (42.6%) than N-CIG without Fe doping (21.1%, Fig. S4†). The high resolution XPS Fe 2p signals (Fig. 2e) with two peaks at 724 eV and 711 eV and no obvious satellite peak at around 719 eV were assigned to Fe $2p_{1/2}$ and Fe $2p_{3/2}$ of Fe_3O_4.[25,31] By careful checking of the TEM images (Fig. S5†), scattered nanoparticles showing a clear lattice fringe with an inter-planar spacing of 0.298 nm were found, in good agreement with the (220) crystal face of Fe_3O_4.[32] Inductively coupled plasma mass spectroscopy (ICP-MS) analysis showed a relatively low iron content of ~1.51 wt% in the Fe–N-CIG sample (Fig. S3†). The N_2 adsorption–desorption isotherm and the accordingly calculated pore size distribution of the as-prepared Fe–N-CIG are given in Fig. 2f. These data revealed a type IV isotherm with a H_3 hysteresis loop,[33] indicating the presence of predominant mesopores and slit shaped pores. After the intercalation of CNS, Fe–N-CIG showed a significantly increased BET specific surface area (457 $m^2\ g^{-1}$) compared to Fe–N-G (202 $m^2\ g^{-1}$, Fig. S6†) for which no CNS intercalation was present.

Electrochemical measurements on both static and rotating disk electrodes (RDE) were employed to characterize the ORR kinetics of different catalysts. Fig. 3a shows cyclic voltammograms (CVs) on static glassy carbon electrodes (GCEs) loaded with Fe–N-G, Fe–N-CIG, and commercial Pt/C (20 wt%), respectively, in an unstirred N_2 or O_2 saturated 0.1 M KOH aqueous solution. A potential scan rate of 10 mV s^{-1} in the range of 0.05–1.25 V *versus* reversible hydrogen electrode (RHE) was employed for all CV tests. The CV curve of the Fe–N-CIG loaded electrode exhibited a much higher ORR peak than those of the Fe–N-G and commercial Pt/C catalysts. In Fig. 3b, well-defined steady state diffusion-limiting currents following mixed kinetic-diffusion regions were observed on the linear sweep voltammetry (LSV) curves of the Fe–N-CIG coated RDE under various rotation speeds from 400 to 1600 rpm. The linearity of the Koutecky–Levich plots based on the RDE data and the near parallelism of the fitting lines suggested first-order reaction kinetics towards dissolved oxygen. The slopes of the Koutecky–Levich plots at different potentials gave an average electron transfer number of 4.0 for the Fe–N-CIG catalyst (inset of

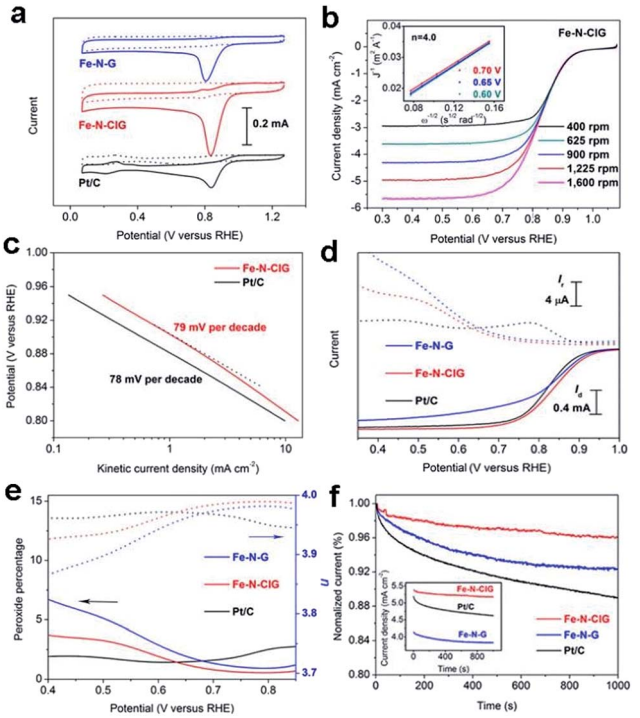

Fig. 3 Electrochemical ORR tests of the as-obtained materials. (a) CV curves of the Fe–N-G (~0.23 mg cm^{-2} loading), Fe–N-CIG (~0.23 mg cm^{-2}) and Pt/C (20 wt% Pt on Vulcan XC-72, ~0.1 mg cm^{-2}) catalysts in N_2-saturated (dotted lines) and O_2-saturated (solid lines) 0.1 M KOH solutions, respectively. (b) Rotating disk electrode (RDE) voltammograms of Fe–N-CIG in O_2-saturated 0.1 M KOH at different rotation speeds. The inset in (b) shows corresponding Koutecky–Levich plots at different potentials. (c) Tafel plots of the Fe–N-CIG and Pt/C catalysts. (d) Rotating ring-disk electrode (RRDE) voltammograms recorded for Fe–N-G, Fe–N-CIG, and Pt/C catalysts in O_2-saturated 0.1 M KOH at 1600 rpm. Solid and dotted curves correspond to the disk and ring currents, respectively. (e) Peroxide yields (solid lines) and corresponding electron transfer numbers (*n*) (dotted lines) of the Fe–N-G, Fe–N-CIG and Pt/C catalysts as a function of applied potential, derived from the RRDE data in (d). (f) Chronoamperometric responses of Fe–N-G, Fe–N-CIG and Pt/C loaded RDEs kept at 0.7 V *versus* RHE in O_2-saturated 0.1 M KOH electrolytes at 1600 rpm, showing an improved stability for the Fe–N-CIG catalyst. The inset shows the chronoamperometric data before normalization.

Fig. 3b), which was larger than that of Fe–N-G (n = 3.95) (Fig. S7†). The excellent ORR performance of the Fe–N-CIG was also evidenced from its Tafel slope of 79 mV per decade in 0.1 M KOH at low overpotentials, similar to commercial Pt/C (78 mV per decade) (Fig. 3c). Rotating ring-disk electrode (RRDE, with a Pt ring electrode) voltammetry was further used to monitor the formation of peroxide (HO_2^-) by-products during the ORR at the catalyst-loaded disk electrode (Fig. 3d). The measured HO_2^- yields were below 7.0% and 4.0% for Fe–N-G and Fe–N-CIG, respectively, through the potential range of 0.4–0.80 V, giving corresponding electron transfer (ET) numbers of ~3.95 and ~3.98 (Fig. 3e). The ET numbers obtained from the RRDE experiments coincided well with those from the Koutecky–Levich plots, suggesting that the ORRs on the Fe–N-CIG and Fe–N-G catalysts were governed by 4e pathways. The high ORR activity of the Fe–N-CIG was also inferred from its half-wave potential (~0.84 V) of the RDE voltammogram (Fig. 3d), which was even more positive than that of the Pt/C catalyst (~0.82 V). In addition, Fe–N-CIG had a higher limiting current than Fe–N-G (Fig. 3d) under the same catalyst loading,‡ implying that the intercalated architecture of Fe–N-CIG could offer more active sites for the ORR. Moreover, the steady-state voltammetric ORR curves on Fe–N-CIG, iron and nitrogen codoped carbon nanospheres (Fe–N–CNS), nitrogen-doped graphene (N-G), nanocarbon-intercalated nitrogen-doped graphene (N-CIG), and Fe–N-G loaded rotating disk electrodes (RDEs) at 1600 rpm are compared in Fig. S8.† On the other hand, the Fe–N-CIG also exhibited a superior electrochemical stability at a constant polarizing potential of 0.7 V in 0.1 M KOH, with a very small current decay (4%) over 1000 s of continuous running (Fig. 3f). In contrast, the Pt/C catalyst exhibited a 12% decrease of its activity under the same conditions, which would prohibit its long-term use.

In addition to the ORR tests, we evaluated the Fe–N-CIG and Fe–N-G catalysts for their oxygen evolution reaction (OER) activities in 0.1 M KOH. The Fe–N-CIG loaded RDE (0.38 mg cm^{-2}) produced higher OER current and more negative onset potential than Fe–N-G, N-CIG and Pt/C (Fig. 4a). In the meantime, the Fe–N-CIG exhibited a lower Tafel slope (96 mV dec^{-1}) compared to that of both Fe–N-G (146 mV dec^{-1}) and N-CIG (180 mV dec^{-1}) (Fig. 4b). The electron transfer properties of the Fe–N-CIG and Fe–N-G electrodes were further characterized by electrochemical impedance spectroscopy (EIS). As shown in Fig. 4c, the Fe–N-CIG had a smaller semicircle part in the EIS Nyquist plot than Fe–N-G, indicating a lower electron-transfer resistance at the catalyst–electrolyte interface.[34,35] Furthermore, we compared Fe–N-CIG with commercially available IrO_2 (Sigma, ~0.2 mg cm^{-2} loading) for their OER activities in 0.1 M KOH at room temperature (Fig. 4d). The onset potential of Fe–N-CIG was estimated to be ~1.4 V, corresponding to a negligible overpotential of ~170 mV (at least 100 mV lower than that of iridium oxide). Moreover, we compared the overpotentials for different catalysts at a current density of 10.0 mA cm^{-2} (inset of Fig. 4d), which indicated an obviously lower potential for Fe–N-CIG (0.39 mV) than for IrO_2 (0.46 mV). Importantly, the Fe–N-CIG exhibited excellent durability with insignificant performance loss under constant polarization at 1.67 V (where the current density was about 10 mA cm^{-2}) (Fig. 4e) or after 100 cycles of consecutive CV scans (Fig. 4f). This might be attributed to the unique 3D structure and the high mechanical stability of the carbon nanosphere intercalated graphene materials. The above results clearly demonstrated that the noble-metal-free Fe–N-CIG hybrid is an excellent bifunctional catalyst for both oxygen reduction and evolution reactions.

Theoretical and experimental studies[22,36,37] have pointed out that N doping can promote both the ORR and OER, and Fe–N_x interactions can mimic an Fe-porphyrin coordination for the ORR.[38,39] As well, oxide forms of first row transition metals including Fe are catalysts for the OER.[40] Consistent with our XPS analysis, several groups have found that transition metals can facilitate the incorporation of active N-containing functionalities into graphitic carbon at high temperature and increase catalytic activities.[10,41] Moreover, the Fe–N-CIG showed a higher

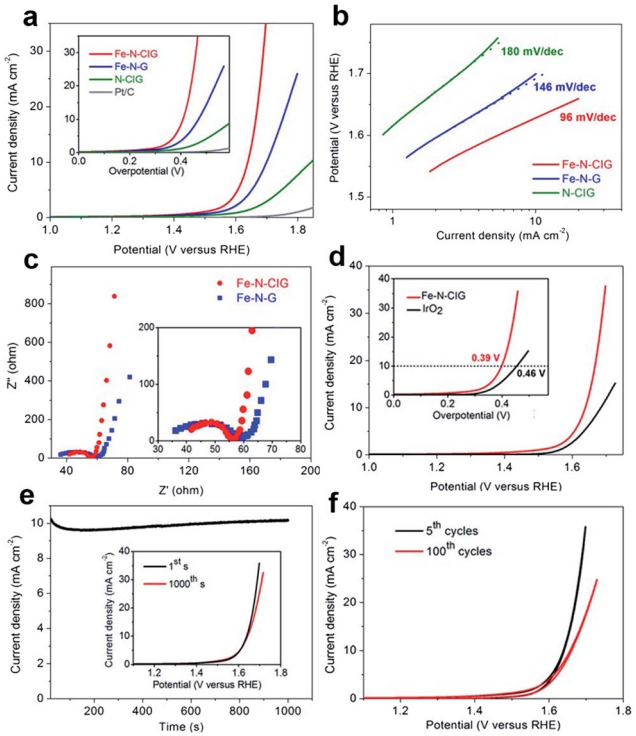

Fig. 4 Electrochemical OER and impedance tests of the as-obtained materials. (a) iR-corrected OER voltammograms of Fe–N-G, Fe–N-CIG, N-CIG, and Pt/C loaded glassy carbon RDEs at 1600 rpm. (b) Tafel plots based on the OER data in (a). (c) Nyquist plots of electrochemical impedance spectra (EIS) for Fe–N-G and Fe–N-CIG; the inset shows magnified semicircle domains of the EIS curves. (d) A comparison of iR-corrected OER voltammograms between Fe–N-CIG and commercial IrO_2 catalysts on glassy carbon RDEs at 1600 rpm. (e) Chronoamperometric response of Fe–N-CIG continuously recorded for 1000 s; the inset shows iR-corrected OER voltammograms after 1 and 1000 s polarizations. (f) iR-corrected OER cyclic voltammograms of Fe–N-CIG corresponding to the 5th and 100th CV cycles. The insets in (a) and (d) are replotted current density curves *versus* overpotential. See Fig. S9† for details of the iR correction.

ratio of pyridinic N than N-CIG. It has been reported that pyridinic N at a graphitic edge is critical for electrocatalysis.[42,43] Therefore, the significantly enhanced ORR and OER activities of Fe–N-CIG could be attributed to three major reasons (Fig. 1). Firstly, the existence of interplanar carbon nanospheres results in a large spacing between two graphene nanosheets, which avoids a serious re-stacking (induced by π electron interactions) of graphene layers and facilitates the N doping reaction. Secondly, the increased distance between N-doped graphene planes makes the catalytically active sites (N, Fe_3O_4, and possibly FeN_x) on the graphene surface easily accessible to ORR and OER related species. Thirdly, the high conductivity of the carbon nanospheres bridging adjacent graphene planes guaranteed efficient electron transport between different graphene layers.

Conclusions

In summary, surprisingly high ORR and OER activities were simultaneously achieved when conductive nanocarbons were intercalated into nitrogen-doped graphene nanosheets containing trace amounts of iron (Fe–N-CIG). The Fe–N-CIG exhibited an improved ORR activity and a superior stability in an alkaline solution, in comparison with noble Pt catalysts. In addition to the ORR, the Fe–N-CIG also showed an excellent activity towards water oxidation (OER), with an onset potential at least 100 mV lower than that of the commercial iridium oxide catalyst. This enables a potential application of the easily fabricated Fe–N-CIG as a dual-functional electrocatalyst for oxygen electrochemistry towards unitized regenerative fuel cells (URFCs) and rechargeable metal–air batteries, which is important for a variety of energy technologies and applications. The nanocarbon intercalation strategy we developed should be adaptable to other two dimensional nanomaterials towards improved performance. Our work opens up a new avenue for the development of energy-conversion-oriented catalytic materials based on earth-abundant elements.

Note after first publication

This article replaces the version published on 15 December 2015, to clarify the conclusions regarding the ORR activity of the Fe–N-CIG sample. In the original version, SEM images in Fig. 2 (a and b) showed stacked lamellar structures. This result was later found to be due to an error in the sample preparation, and as such the original conclusions regarding the direct relationship between the improved ORR activity of Fe–N-CIG material and the intercalation of carbon nanospheres were no longer valid. In the current version Fig. 2 (a and b) have been replaced with corrected SEM images, and the related discussion in the sentence beginning "The SEM and TEM data…" has been revised accordingly. In addition, the original version showed the Fe–N-CIG samples had superior ORR activity to Fe–N-G samples. Subsequently it was found that some of the prepared Fe–N-G samples revealed similar ORR activities to Fe–N-CIG. A new figure has been included in the Supplementary Information (Fig. S10†) showing additional data on the ORR performance of these Fe–N-G samples, and a footnote has been added discussing the implications of these results.

Acknowledgements

S. M. acknowledges financial support from the National Basic Research Program of China (973 Program, 2012CB215504) and the NSFC (51372186). Z. D. is grateful to financial support from NSFC (Grants 21273214, 21425521, and 21521001), Hefei Center for Physical Science and Technology (2014FXCX010), and the Collaborative Innovation Center of Suzhou Nano Science and Technology. D. H. is supported by the Royal Society for a Newton International Fellow, the China Postdoctoral Science Foundation (2014M551811), the State Key Laboratory of Advanced Technology for Material Synthesis and Processing (Wuhan University of Technology) (No. 2014-KF-9), and the Fundamental Research Funds for the Central Universities.

Notes and references

‡ Note: subsequently, we found that the Fe–N-G sample prepared in some rare batches exhibited a good ORR activity (Fig. S10†). This implies another potential factor during the sample preparations (besides the carbon sphere intercalation) can improve the activity of Fe–N-G, which was, however, not as reproducible and reliable as the Fe–N-CIG sample. Therefore, doping with conductive carbon nanospheres (Fe–N-CIG) is still an excellent and very reliable way to achieve an improved ORR activity of Fe–N-G. This phenomenon definitely deserves a future investigation towards a potentially new activity-enhancing factor.

1 M. Armand and J. M. Tarascon, *Nature*, 2008, **451**, 652.
2 B. Dunn, H. Kamath and J. M. Tarascon, *Science*, 2011, **334**, 928.
3 N. S. Lewis and D. G. Nocera, *Proc. Natl. Acad. Sci. U. S. A.*, 2006, **103**, 15729.
4 Y. Gorlin and T. F. Jaramillo, *J. Am. Chem. Soc.*, 2010, **132**, 13612.
5 A. A. Gewirth and M. S. Thorum, *Inorg. Chem.*, 2010, **49**, 3557.
6 R. Bashyam and P. Zelenay, *Nature*, 2006, **443**, 63.
7 G. Wu, K. L. More, C. M. Johnston and P. Zelenay, *Science*, 2011, **332**, 443.
8 Y. G. Li, P. Hasin and Y. Y. Wu, *Adv. Mater.*, 2010, **22**, 1926.
9 M. W. Kanan and D. G. Nocera, *Science*, 2008, **321**, 1072.
10 Y. Y. Liang, Y. G. Li, H. L. Wang, J. G. Zhou, J. Wang, T. Regier and H. J. Dai, *Nat. Mater.*, 2011, **10**, 780.
11 C. Chen, Y. J. Kang, Z. Y. Huo, Z. W. Zhu, W. Y. Huang, H. L. Xin, J. D. Snyder, D. G. Li, J. A. Herron, M. Mavrikakis, M. F. Chi, K. L. More, Y. D. Li, N. M. Markovic, G. A. Somorjai, P. D. Yang and V. R. Stamenkovic, *Science*, 2014, **343**, 1339.
12 M. Winter and R. J. Brodd, *Chem. Rev.*, 2004, **104**, 4245.
13 S. I. Choi, S. F. Xie, M. H. Shao, J. H. Odell, N. Lu, H. C. Peng, L. Protsailo, S. Guerrero, J. Park, X. H. Xia, J. G. Wang, M. J. Kim and Y. N. Xia, *Nano Lett.*, 2013, **13**, 3420.
14 B. Lim, M. J. Jiang, P. H. C. Camargo, E. C. Cho, J. Tao, X. M. Lu, Y. M. Zhu and Y. N. Xia, *Science*, 2009, **324**, 1302.
15 S. Trasatti, *J. Electroanal. Chem.*, 1980, **111**, 125.
16 S. Trasatti, *Electrochim. Acta*, 1984, **29**, 1503.
17 K. P. Gong, F. Du, Z. H. Xia, M. Durstock and L. M. Dai, *Science*, 2009, **323**, 760.
18 R. L. Liu, D. Q. Wu, X. L. Feng and K. Müllen, *Angew. Chem., Int. Ed.*, 2010, **49**, 2565.
19 L. T. Qu, Y. Liu, J. B. Baek and L. M. Dai, *ACS Nano*, 2010, **4**, 1321.
20 X. C. Wang, K. Maeda, A. Thomas, K. Takanabe, G. Xin, J. M. Carlsson, K. Domen and M. Antonietti, *Nat. Mater.*, 2009, **8**, 76.
21 S. Mao, Z. H. Wen, T. Z. Huang, Y. Hou and J. H. Chen, *Energy Environ. Sci.*, 2014, **7**, 609.
22 J. T. Zhang, Z. H. Zhao, Z. H. Xia and L. M. Dai, *Nat. Nanotechnol.*, 2015, **10**, 444.
23 S. Chen, J. J. Duan, M. Jaroniec and S. Z. Qiao, *Adv. Mater.*, 2014, **26**, 2925.
24 K. Novoselov, E. McCann, S. Morozov, V. I. Fal'ko, M. Katsnelson, U. Zeitler, D. Jiang, F. Schedin and A. Geim, *Nat. Phys.*, 2006, **2**, 177.
25 Z. S. Wu, S. B. Yang, Y. Sun, K. Parvez, X. L. Feng and K. Müllen, *J. Am. Chem. Soc.*, 2012, **134**, 9082.
26 Y. G. Li, W. Zhou, H. L. Wang, L. M. Xie, Y. Y. Liang, F. Wei, J. C. Idrobo, S. J. Pennycook and H. J. Dai, *Nat. Nanotechnol.*, 2012, **7**, 394.
27 Y. Y. Liang, H. L. Wang, J. G. Zhou, Y. Y. Li, J. Wang, T. Regier and H. J. Dai, *J. Am. Chem. Soc.*, 2012, **134**, 3517.
28 S. Chen, J. Duan, M. Jaroniec and S. Z. Qiao, *Angew. Chem., Int. Ed.*, 2013, **52**, 13567.
29 P. Wu, H. F. Lv, T. Peng, D. P. He and S. Mu, *Sci. Rep.*, 2014, **4**, 3968.
30 R. Arrigo, M. Hävecker, R. Schlögl and D. S. Su, *Chem. Commun.*, 2008, 4891.
31 T. Fujii, F. M. F. de Groot, G. A. Sawatzky, F. C. Voogt, T. Hibma and K. Okada, *Phys. Rev. B*, 1999, **59**, 3195.
32 Y. Q. Liu, Y. Zhang and J. Wang, *CrystEngComm*, 2014, **16**, 5948.
33 S. M. Paek, E. Yoo and I. Honma, *Nano Lett.*, 2009, **9**, 72.
34 M. D. Stoller, S. Parl, Y. Zhu, J. An and R. S. Ruoff, *Nano Lett.*, 2008, **8**, 3498.
35 D. P. He, Y. L. Jiang, H. F. Lv, M. Pan and S. C. Mu, *Appl. Catal. B: Environ.*, 2013, **132–133**, 379.
36 L. Wang, F. X. Yin and C. X. Yao, *Int. J. Hydrogen Energy*, 2014, **39**, 15913.
37 M. T. Li, L. P. Zhang, Q. Xu, J. B. Niu and Z. H. Xia, *J. Catal.*, 2014, **314**, 66.
38 A. Zitolo, V. Goellner, V. Armel, M. T. Sougrati, T. Mineva, L. Stievano, E. Fonda and F. Jaouen, *Nat. Mater.*, 2015, **14**, 937.
39 Y. S. Zhu, B. S. Zhang, X. Liu, D. W. Wang and D. S. Su, *Angew. Chem., Int. Ed.*, 2014, **53**, 10673.
40 A. J. Esswein, M. J. McMurdo, P. N. Ross, A. T. Bell and T. D. Tilley, *J. Phys. Chem. C*, 2009, **113**, 15068.
41 V. Nallathambi, J. W. Lee, S. P. Kumaraguru, G. Wu and B. N. Popov, *J. Power Sources*, 2008, **183**, 34.
42 J. Liu, X. J. Sun, P. Song, Y. W. Zhang, W. Xing and W. L. Xu, *Adv. Mater.*, 2013, **25**, 6879.
43 W. Xia, J. Masa, M. Bron, W. Schuhmann and M. Muhler, *Electrochem. Commun.*, 2011, **13**, 593.

